PREPRINT-REIHE
ANGEWANDTE MATHEMATIK
des Departments Mathematik

Friedrich-Alexander-Universität Erlangen-Nürnberg

# Beyond Kozeny-Carman: Predicting the permeability in porous media

*von*

*R. Schulz, N. Ray, S. Zech, A. Rupp & P. Knabner*

No. 403 2019

Department Mathematik
– Bereich Modellierung, Simulation, Optimierung –
Cauerstraße 11
91058 Erlangen

Geschäftsstelle:

Tel.: +49 9131 85-67063
Fax: +49 9131 85-67065

Internet: http://www.am.uni-erlangen.de

ISSN 2194-5127, 20.03.2019, No. 403

# BEYOND KOZENY-CARMAN: PREDICTING THE PERMEABILITY IN POROUS MEDIA

RAPHAEL SCHULZ, NADJA RAY, SIMON ZECH, ANDREAS RUPP, AND PETER KNABNER

Abstract. Various processes such as heterogeneous reactions or biofilm growth alter a porous medium's underlying geometric structure. This significantly affects its hydrodynamic parameters, in particular the medium's effective permeability. An accurate, quantitative description of the permeability is, however, essential for predictive flow and transport modeling. Well-established relations such as the Kozeny-Carman equation or power law approaches including fitting parameters relate the porous medium's porosity to a scalar permeability coefficient. Opposed to this, upscaling methods directly enable calculating the full, potentially anisotropic, permeability tensor. As input only the geometric information in terms of a representative elementary volume is needed. To compute the porosity-permeability relations, supplementary cell problems must be solved numerically on this volume and their solutions must be integrated. We apply this approach to provide easy to use quantitative porosity-permeability relations that are based on representative single grain, platy, blocky, prismatic soil structures, porous networks, and real geometries obtained from CT-data. As a discretization method, we use discontinuous Galerkin method on structured grids. To make the relations explicit, interpolation of the obtained data is used. We compare the outcome with the well-established relations and investigate the ranges of the validity. From our investigations, we conclude whether Kozeny-Carman type or power law type porosity-permeability relations are more reasonable for various prototypic representative elementary volumes. Finally, we investigate the impact of a microporous solid matrix onto the permeability.

*Keywords:* Kozeny Carman, permeability, power law, upscaling

## 1. Introduction

Flow and transport processes through porous media have an incredible long research history. Nevertheless, even the basic and most commonly used model equations and their parameters are still under investigation. Fluid flow through a porous medium is classically described by Darcy's law

$$u + \tfrac{1}{\mu}\mathbb{K}\nabla p = f$$

with Darcy velocity $u$, pressure $p$, viscosity $\mu$, effective permeability $\mathbb{K}$, and external force term $f$ [19].

The effective tensor $\mathbb{K}$ is the essential input to the model since it contains all the information that is specific for the considered porous medium. However, it is very difficult to characterize in (natural) porous media - even if it is assumed to be represented by a scalar $K$. Consequently, formulae in terms of simple features of the porous medium, e.g. the porosity, are frequently used.

In the context of diffusion in porous systems, Quintard states that porosity is the essential parameter for unconsolidated isotropic media [40]. Along this line, porosity-permeability models such as the Kozeny-Carman equation are often used, even for more general situations. The composition and structure of an arbitrary porous medium can, however, not be accounted for by porosity variations only. Changes in particle distribution or grain shape and size modify the tortuosity and connectivity of the pore space and therefore the bulk response of the medium. Consequently, models including shape factors or fitting parameters are used and may have very good approximation properties when fitted to experimental data. The main drawback of this approach is that the model parameters often have no direct connection to the underlying porous medium structure, have no physical interpretation, or are hard or even impossible to measure. In terms of applicability, explicit porosity-permeability relations without any artificial parameters are most desirable. With our research we contribute to this point. Based on representative elementary volumes with representative soil structures, we calculate quantitative porosity-permeability models that are easy to use and are valid in the whole range of porosity, cf. Section 5.2. From our investigations, we conclude whether Kozeny-Carman type or power law type porosity-permeability relations are more reasonable for various prototypic representative elementary volumes.

In this paper, we first review well-established relations for the scalar permeability in terms of porosity, cf. Section 2. Secondly, we state standard results from upscaling theory potentially including the impact of a microporous solid matrix to the permeability, cf. Section 3. Integrating the solutions of auxiliary cell problems allows calculating the full, potentially anisotropic, permeability tensor. In Section 4, we introduce the numerical methods and the representative geometries. We numerically evaluate the permeability in terms of porosity in Section 5.1 and 5.2 for a real porous media from CT images and the representative geometries, respectively. Additionally, explicit functional relations are derived via interpolation of the obtained data. We compare the outcome with the well-established relations and investigate the ranges of the validity. Ultimately, the impact of a microporous solid matrix to the permeability is investigated in Section 5.3. This illustrates that even the full geometrical information may be insufficient to deduce the effective permeability tensor of the medium.

## 2. Well-established functional relations between permeability and porosity

Finding suitable functional relations between the porosity $\theta$ (ratio of pore space to total volume) and the effective permeability tensor $\mathbb{K}$ or rather its scalar representative $K$ has been the topic of research for several decades. A recent review is found in [26]. The most commonly used porosity-permeability relations are the Kozeny-Carman equation (1) and power laws (4). Kozeny [30] originally proposed

$$K = \frac{c_0}{\sigma_1^2}\theta^3$$

as a functional dependence between the porosity and the permeability for a porous medium consisting of straight tubes. The so-called Kozeny's constant $c_0$ depends slightly on the geometrical cross-section of the tubes and in [5] values of $c_0$ are reported for a circle $c_0 = 0.5$, a square $c_0 = 0.562$, a triangle $c_0 = 0.597$, and a strip $c_0 = 0.667$. $\sigma_1$ denotes the specific surface per unit bulk volume.

Carman [10] reformulated the Kozeny equation as

$$K = \frac{c_0}{\sigma^2}\frac{\theta^3}{(1-\theta)^2} \tag{1}$$

by replacing $\sigma_1$ with the specific surface $\sigma$ with respect to the unit volume of the solid matrix, i.e. it holds $\sigma_1 = (1-\theta)\sigma$ [5, (2.6.3)]. Furthermore, Carman 1939 (cf. [15]) tried to take into account that porous media generally do not consist of straight tubes but of irregularly shaped particles. To include this fact he estimated the Kozeny constant $c_0$ to be equal to $\frac{1}{5}$ giving the best agreement with experiments. In [36] values for the Kozeny constant are listed and studies determining the Kozeny constant are reviewed. Further experiments suggest that the Kozeny coefficient $c_0 = c_0(\theta)$ depends on the porosity $\theta$ itself. In more detail, it was empirically shown that the quotient $(\frac{c_0}{\sigma^2})/(\frac{\theta^3}{(1-\theta)^2})$ does not remain constant for decreasing porosity $\theta$ but increases, cf. [11]. Relations of the Kozeny constant with respect to porosity are listed in [36]. Carman concludes that equation (1) is not satisfied for very small porosities, e.g. for clays [11]. In [12] the limitation of (1) for coarse materials in which the Darcy regime is no longer given is additionally discussed.

Due to the general complexity of porous media, the same porosities may induce different effective permeabilities, cf. [21] and Section 5.2 for a numerical illustration. To overcome this drawback and relax the widely taken assumption that a porous medium consists of straight tubes, there is already numerous research taking additionally geometric features such as the tortuosity, mean particle size, or grain size into account. The tortuosity is defined as the ratio of the average traveling length per unit length. Incorporating the tortuosity into the Kozeny-Carman equation (1) yields

$$K = \frac{c_0}{\tau^2\sigma^2}\frac{\theta^3}{(1-\theta)^2}\ ,$$

cf. [21, 50]. The porosity is often related to the tortuosity via the resistivity factor $F$, the constrictivity, or model parameters that may be calibrated with experimental data. Archies law $F = \frac{A}{\theta^m}$ (with parameters $A, m$) then yields the following porosity-tortuosity relation

$$\tau^2 = (F\theta)^n = (A\theta^{(1-m)})^n \tag{2}$$

with parameters $A, m$, and $n$, cf. [48]. For sands and muds this relation is used with $n = 1$. Then the empirical coefficient $A$ varies in the range between 0.6 and 2 and the tortuosity factor $m$ within 1 to 4, see [17]. Further porosity-tortuosity relations are summarized in [1, 23, 39, 48]. In [39] simple expressions for the tortuosity depending on the porosity and a further parameter describing the average distance to bypass solid obstacles are proposed. In [1] a quite complex tortuosity-permeability relation for spherical porous media was derived. Since it is challenging to determine the tortuosity via lengths of streamlines, [20] proposed a method which allows calculating the tortuosity directly from the fluid velocity field. Finally, [23] has critically reviewed the vast number of tortuosity models. As main drawback of the proposed models, this article stated that they are all distinct and not comparable due to their distinct derivation namely empirically, analytically, and numerically. Following [8], beside the porosity and tortuosity also a characteristic hydraulic length (describing the effective hydraulic pore radius) and a constriction factor (characterizing the fluctuation of local hydraulic radii) should be considered for an appropriate formula predicting permeability of a porous media.

Alternatively, the Kozeny-Carman equation (1) is reformulated in terms of the mean particle size $d$ [51] to include further geometric information. For spherical grains of constant size it holds $d = \frac{6}{\sigma}$ leading with $c_0 = \frac{1}{5}$ to

$$K = \frac{d^2}{180} \frac{\theta^3}{(1-\theta)^2} \ .$$

For circles, squares, crosses (and cylinders) on the other hand, it holds $d = \frac{4}{\sigma}$ and thus

$$K = \frac{d^2}{80} \frac{\theta^3}{(1-\theta)^2} \ .$$

cf. [58]. In more general geometrical settings a shape factor $f(s)$ with $f(s)d^2 = \frac{c_0}{\sigma^2}$ is introduced and hence

$$K = f(s) d^2 \frac{\theta^3}{(1-\theta)^2}$$

holds, cf. [5, 51].

A large number of further permeability models in terms of the grain size $d_{10}$ ($d_x$ denotes the grain size such that $x$% of the solid grains are finer than $d_x$) instead of the mean grain size are reviewed in [14]. In addition to the Hazen relation, Kozeny-Carman type equations are formulated:

$$\begin{aligned} K &= C_H (d_{10})^2 && \text{(Hazen 1911)} \ , \\ K &= 1.2 C_U^{0.735} d_{10}^{0.89} \tfrac{\theta^3}{(1-\theta)^2} && \text{(Shahabi 1984)} \ , \\ K &= 2.4622 \left( d_{10}^2 \tfrac{\theta^3}{(1-\theta)^2} \right)^{0.7825} && \text{(Chapuis 2004)} \ . \end{aligned} \tag{3}$$

The Hazen formula is valid for $0.1\text{mm} < d_{10} < 3\text{mm}$ with the Hazen empirical coefficient $C_H$ taking values between 1 and 1,000, but is usually assumed to be 100, cf. listing and references in [12]. The parameter $C_U := \frac{d_{60}}{d_{10}}$ is the coefficient of uniformity. Several experimental studies of the grain size impact on the permeability showed that using $d_{10}$ is a good choice compared to e.g. $d_{17}$, $d_{20}$ or $d_{50}$ (also used in other formulae). Moreover, each of the above models in (3) is reasonable only if the parameters $\theta, d_{10}$ and $C_U$ satisfy specific conditions, cf. [14]. E.g. the last relation of Chapuis 2004 yields good prediction for natural soil with $d_{10} > 3\text{mm}$ and $0.23 < \theta < 0.5$.

In addition to the Kozeny-Carman relation and its variations discussed above, power law models are available for the permeability with fitting parameters $\lambda, \eta$ [26].

$$\tfrac{K}{K_0} = \left( \tfrac{\theta}{\theta_0} \right)^\eta \quad \text{or} \quad K = \lambda \theta^\eta \ , \tag{4}$$

where $K_0$ and $\theta_0$ denote the initial or a reference value of permeability and porosity, respectively. Although 3 is a common choice for $\eta$, the values of $\eta$ strongly depend on the underlying processes which change the pore space. Smith et al. [26, 49], who investigate the dissolution of carbonate rocks suggest $\eta = 3$ for homogeneous and $\eta$ between 6 and 8 for heterogeneous rocks. Menke even proposes values of $16.2 < \eta < 23.8$ for heterogeneous media [32]. Bernabé et al. [26, 9] determine $\eta$ between 2.5 and 3 for plastic compaction, $\eta > 10$ for chemical alteration, and $\eta > 20$ for mineral dissolution. Although power laws are easy to use relations, we emphasize that power laws or especially the Verma-Pruess relation (see below and [26]) do not tend to infinity for $\theta \to 1$. Thus it is necessary to verify for each application separately whether these models replicate the real behavior, cf. Section 5.2.

Along these lines, there is an unmanageable number of formulae for the effective permeability depending not only on the porosity, but also on numerous fitting parameters and physical variables incorporating geometrical information into the models. However, in terms of applicability low parameter models being particularly independent of hard to measure input are most desirable. Moreover, many of the cited models are derived from fitting to data and are often only valid in a small range of porosity, due to experimental constraints. The smaller the range, the better approximations may be obtained even with linear models and the more sophisticated it is to yield accurate approximation qualities with power laws. For most soils the range of porosity lies between 0.3 and 0.7 [34] and idealized porous media are often considered to represent the soil. Consequently, porosity ranges related to sphere packings are of particular interest. Uniform packed spheres have porosities between 0.26 and 0.48. The porosity for densest packings range from 0.26 to 0.32 for cubic body centered packings. Random packings have porosity ranges between 0.3 and 0.35 and yield good approximations for sandy soils. Although polydisperse sands could theoretically fall to porosities below 0.26, this is improbable and porosities of 0.3-0.35 are obtained [34]. However, porous rocks such as sandstone may have very low porosities ($< 0.3$) and peat soils contrarily have porosities up to 0.8-0.9 [34]. In this sense the whole range of porosities is relevant and thus is investigated within this research.

A further drawback of functional relations stated above is that the permeability degenerates only for $\theta = 0$. This model assumption is a very strong restriction and not reasonable for most geometric settings. Consequently, the following model improvement is considered throughout this research: $\theta$ is replaced by $\theta - \hat{\theta}$ for $\theta \geq \hat{\theta}$ and $K = 0$ otherwise, cf. also the Verma-Pruess relation (8) [26] or [53, 43] in the context of porosity-diffusion relations. The value of $\hat{\theta}$ is analytically deduced from the specifically chosen geometry, cf. Table 1.

Additionally, we emphasize the fundamental drawback that the Kozeny-Carman equation (1) as well as their variations, the power law model (4) and all models listed in (3) refer to scalar coefficients rather than to the full tensors. This simplification is only verified for isotropic porous media; compare Remark 1 and 2 in Section 3 and the numerical illustrations in Section 5.2. However, porous media and thus also the corresponding effective permeability tensor are often anisotropic, cf. [15, 12]. In Section 3, we state some mathematical theory which enables computing the full permeability tensor on the prescribed geometry of a representative elementary volume. The simulation outcomes are discussed for different representative geometries in Section 5 and made quantitative by interpolating the obtained data. In doing so the following variants of the Kozeny-Carman and Verma-Pruess equations (power law) potentially including degeneration are considered:
Kozeny-Carman equation for given $\hat{\theta}$ and with one free parameter $\lambda$

$$K_{KC1}(\theta) = \lambda \frac{(\theta - \hat{\theta})^3}{(1-\theta)^2}\,, \qquad \theta \geq \hat{\theta} \tag{5}$$

Kozeny-Carman equation with two free parameters $\lambda, \beta$

$$K_{KC2}(\theta) = \lambda \frac{(\theta - \hat{\theta})^3}{(1-\theta)^\beta}\,, \qquad \theta \geq \hat{\theta} \tag{6}$$

Kozeny-Carman equation with three free parameters $\lambda, \beta, \eta$

$$K_{KC3}(\theta) = \lambda \frac{(\theta - \hat{\theta})^\eta}{(1-\theta)^\beta}\,, \qquad \theta \geq \hat{\theta} \tag{7}$$

Verma-Pruess equation (power law) with two free parameters $\lambda, \eta$

$$K_{VP}(\theta) = \lambda \left(\theta - \hat{\theta}\right)^\eta \,. \tag{8}$$

## 3. Mathematical model

If the underlying geometry of a representative elementary volume $Y$ is prescribed, cf. Figure 2 and Figure 3, some mathematical theory is available that makes it possible to calculate the full, potentially anisotropic, tensor $\mathbb{K}$. Starting from mathematical models at the pore scale, an averaging procedure is performed in order to derive effective models. For fluid flow, incompressible Stokes equations are the starting point. Volume averaging [56], two-scale asymptotic expansion [7] or mathematically more rigorously, two-scale convergence [33, 2] may be applied to these equations. As a result of the averaging procedure, Darcy's law as introduced in

Section 1 is derived. The effective tensor $\mathbb{K}$ is given explicitly as the integral over solutions of auxiliary cell problems which are defined on the representative elementary volume. The situation may be extended to the Stokes-Darcy regime at the pore scale, see Section 3.2. This means that the porous matrix is not considered to be a completely inert solid, but also contributes to the flow by its own microporosity. Upscaling in this situation also yields a Darcy-type law and auxiliary cell problems, from which the permeability tensor $\bar{\mathbb{K}}$ may be calculated.

3.1. **Upscaling the Stokes equations to Darcy's law.** The porosity $\theta = \frac{|Y_s|}{|Y|}$ is defined as the volume of the pore space $Y_s = Y \backslash \bar{Y}_d$ with respect to the total volume of the representative elementary volume $Y = \left(-\frac{1}{2}, \frac{1}{2}\right)^n$, where $Y_d$ denotes the solid phase within $Y$, cf Figure 1 (right). The permeability $\mathbb{K}$ in the Stokes regime may be determined using the following homogenization result.

From **Stokes equations** at the pore scale with scaling parameter $\varepsilon > 0$, velocity $u^\varepsilon$, pressure $p^\varepsilon$, and external force term $f = f(x)$

$$
\begin{aligned}
-\varepsilon^2 \mu \Delta u^\varepsilon + \nabla p^\varepsilon &= f && \text{in } \Omega_s^\varepsilon \\
\nabla \cdot u^\varepsilon &= 0 && \text{in } \Omega_s^\varepsilon \\
u^\varepsilon &= 0 && \text{on } \Gamma_{sd}^\varepsilon\ ,
\end{aligned} \tag{9}
$$

where $\Omega_s^\varepsilon$ denotes the pore space and $\Gamma_{sd}^\varepsilon$ the interface (boundary of the solid matrix), cf. Figure 1 (left). **Darcy's law** is deduced via homogenization theory [27]

$$
\begin{aligned}
u + \tfrac{1}{\mu} \mathbb{K} \nabla p &= f && \text{in } \Omega \\
\nabla \cdot u &= 0 && \text{in } \Omega
\end{aligned} \tag{10}
$$

with the effective permeability tensor $\mathbb{K} = (\mathbb{K}_{ij})_{i,j=1}^n$ being determined via

$$
\mathbb{K}_{ij} := \tfrac{1}{|Y|} \int_{Y_s} (\omega_j)_i \, dy \tag{11}
$$

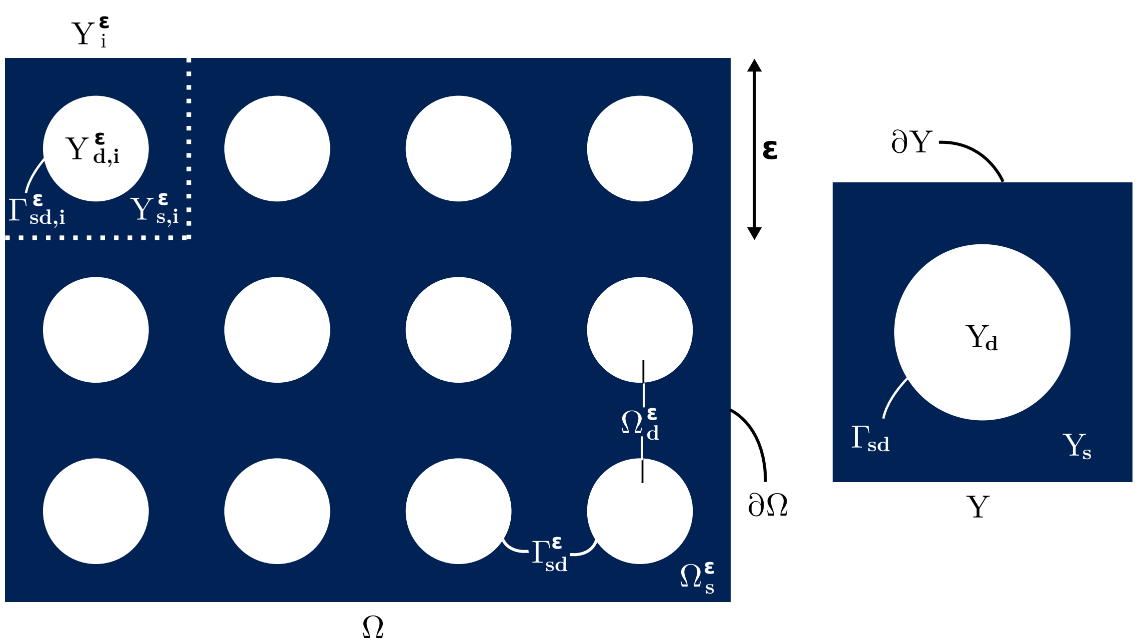


FIGURE 1. *Left:* periodic representation of a porous medium $\Omega$ in 2D with pore space $\Omega_s^\varepsilon$. *Right:* unit cell $Y$ with solid grain $Y_d$, liquid phase $Y_s$, and interface $\Gamma_{sd}$.

with supplementary cell problems in $(\omega_j, \pi_j)$, $j = 1, \dots, n$

$$\left\{\begin{array}{rcll} -\Delta_y \omega_j + \nabla_y \pi_j &=& -e_j & \text{in } Y_s \\ \nabla_y \cdot \omega_j &=& 0 & \text{in } Y_s \\ \omega_j &=& 0 & \text{on } \Gamma_{sd} \\ \omega_j, \pi_j \text{ periodic in } y. &&& \end{array}\right. \tag{12}$$

Hereby, $e_j$ denotes the unit vector in direction $j = 1, ..., n$.

**Remark 1.** *For isotropic media, the effective tensor reduces to a scalar $\mathbb{K} = K\mathbb{E}$ with unity matrix $\mathbb{E}$. Such settings are numerically evaluated and illustrated in Section 5.2, Figure 6. In general, it is difficult to work out analytical solutions of the cell problem* (12)*. However, in case of a tube (see Figure 2) the problem reduces to the Poiseuille flow and thus the analytically determined permeability is equal to $K = \frac{1}{12}\theta^3$, cf.* [4].

3.2. **Upscaling the Stokes-Darcy regime to Darcy's law.** The coupled Stokes-Darcy system at the pore scale with scaling parameter $\varepsilon$ as given in [4] reads

**Stokes equations** in the pore space

$$\begin{array}{rl} -2\mu\varepsilon^2 \nabla \cdot (D u_s^\varepsilon) + \nabla p_s^\varepsilon = f & \text{in } \Omega_s^\varepsilon \\ \nabla \cdot u_s^\varepsilon = 0 & \text{in } \Omega_s^\varepsilon \\ u_s^\varepsilon = 0 & \text{on } \partial\Omega \end{array} \tag{13a}$$

**Darcy equations** in the porous matrix

$$\begin{array}{rl} u_d^\varepsilon + \mu^{-1} \tilde{K} \nabla p_d^\varepsilon = f & \text{in } \Omega_d^\varepsilon \\ \nabla \cdot u_d^\varepsilon = 0 & \text{in } \Omega_d^\varepsilon \end{array} \tag{13b}$$

Beavers-Joseph **interface conditions**

$$\begin{array}{rl} u_s^\varepsilon \cdot \nu_s = u_d^\varepsilon \cdot \nu_s & \text{on } \Gamma_{sd}^\varepsilon \\ 2\nu_s \cdot D u_s^\varepsilon \cdot \tau = -\frac{\alpha}{\varepsilon\sqrt{\tilde{K}}} u_s^\varepsilon \cdot \tau & \text{on } \Gamma_{sd}^\varepsilon \\ 2\mu\varepsilon^2 \nu_s \cdot D u_s^\varepsilon \cdot \nu_s = p_s - p_d & \text{on } \Gamma_{sd}^\varepsilon \end{array} \tag{13c}$$

with velocity $u_s^\varepsilon$ and pressure $p_s^\varepsilon$ in the Stokes region, velocity $u_d^\varepsilon$ and pressure $p_d^\varepsilon$ in the Darcy region, external force term $f = f(x)$, permeability $\tilde{K}$ of the microporous matrix, and Beavers-Joseph interface condition [6] with dimensionless slip coefficient $\alpha$. Moreover, the unit normal $\nu_s$ points into the solid and the tangential vector $\tau$ with length 1 is orthogonal to $\nu_s$. In (13) $D u_s^\varepsilon = \frac{1}{2}\nabla(u_s^\varepsilon + (u_s^\varepsilon)^T)$ is the symmetric gradient.

The mean velocity $\bar{u}$ fulfills Darcy's law and is given as the sum of the mean velocity $\bar{u}_s$ in the Stokes region and the mean velocity $\bar{u}_d$ in the Darcy region, i.e.

$$\begin{array}{rl} \bar{u} = \bar{u}_s + \bar{u}_d = -\frac{1}{\mu}\bar{\mathbb{K}}\nabla p + f & \text{in } \Omega \\ \nabla \cdot \bar{u} = q & \text{in } \Omega \end{array} \tag{14}$$

with effective permeability tensor $\bar{\mathbb{K}} = (\bar{\mathbb{K}}_{ij})_{i,j=1}^n$ given via

$$\bar{\mathbb{K}}_{ij} := \frac{1}{|Y|} \int_{Y_s} (\omega_j^s)_i \, dy + \frac{1}{|Y|} \int_{Y_d} (\omega_j^d)_i \, dy \tag{15}$$

and supplementary cell problems in $(\omega_j^s, \pi_j^s, \omega_j^d, \pi_j^d)$, $j = 1, ..., d$

$$\begin{cases} -2\nabla_y \cdot D\omega_j^s + \nabla_y \pi_j^s &= e_j & \text{in } Y_s \\ \nabla_y \cdot \omega_j^s &= 0 & \text{in } Y_s \\ \mu \tilde{K}^{-1} \omega_j^d + \nabla_y \pi_j^d &= e_j & \text{in } Y_d \\ \nabla_y \cdot \omega_j^d &= 0 & \text{in } Y_d \\ \omega_j^s \cdot \nu_s &= \omega_j^d \cdot \nu_s & \text{on } \Gamma_{sd} \\ 2\nu_s \cdot D\omega_j^s \cdot \tau &= -\frac{\alpha}{\sqrt{\tilde{K}}} \omega_j^s \cdot \tau & \text{on } \Gamma_{sd} \\ 2\nu_s \cdot D\omega_j^s \cdot \nu_s &= \pi_j^s - \pi_j^d & \text{on } \Gamma_{sd} \\ \omega_j^s, \pi_j^s \text{ periodic in } y. \end{cases}$$

**Remark 2.** *For scalar-valued $\tilde{K}$ and isotropic media, the effective tensor $\bar{\mathbb{K}}$ reduces to a scalar $\bar{\mathbb{K}} = \bar{K}\mathbb{E}$ with unity matrix $\mathbb{E}$. Such settings are numerically evaluated and illustrated in Section 5.3, Table 9.*

## 4. Setting and numerical methods

Assumptions on the hard to access microstructure have to be made to apply the mathematical theory introduced in Section 3. In our study, representatives elementary volumes for single grain, platy, blocky, prismatic soil structures, porous networks, or real porous media from CT images are used, cf. Figure 2 and Figure 3. Such geometries often serve as model systems for hypotheses testing. Moreover, due to its tremendous complexity, idealized porous media are frequently used to represent the soil [34]. 2D representatives, e.g. prototypes with rough (potentially structured) planar surfaces, 3D transparent model systems consisting of silica glass beads which facilitate imaging, or model systems from 3D printing techniques allowing to create sophisticated model systems with controlled surface properties and topologies are used [25]. The model systems chosen also mimic artificial model systems that directly arise in technical applications. Examples are microfluidic systems such as 1D analogues of porous media [22] or microwells which allow the precise geometric positing or trapping of cell for cultivation or further studies. The wells may for instance comprise honeycomb structures [28]; recently also 3D porous cubes which facilitate oxygen diffusion have been investigated [41].

The permeability of porous media with specific underlying geometries has been investigated by numerous authors: In [35] a circular geometry is considered and the calculated functional relation between permeability and porosity is fitted to a third order polynomial. In [3], a even more complex situation is considered: In an anisotropic rectangular geometry, the permeability tensor over porosity is calculated, which finally leads to a non monotonic functional relation for the cations. Similarly in [42], different interaction potentials relating rather to van-der Waals-interaction than electric ones are considered and the effective permeability

FIGURE 2. 2D geometries: square, circle, cross of type 1, cross of type 2, rectangle of type 1 with different but constant height, rectangle of type 2, ellipse, tube; fluid in blue, solid in white

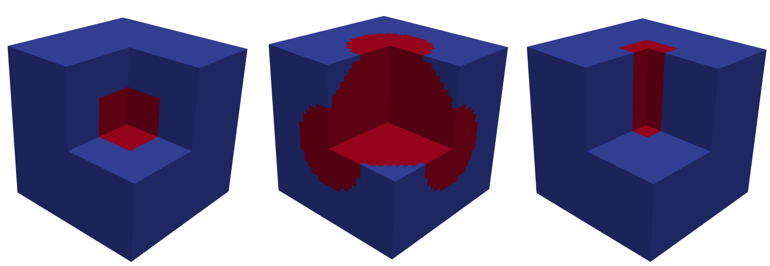

FIGURE 3. 3D geometries cube, sphere and tube; fluid in blue, solid in red.

| Geometry | $\hat{\theta}$ |
|---|---|
| Square | 0 |
| Circle | $1-\frac{\pi}{4}$ |
| Cross (type 1) | 0.64 |
| Cross (type 2) | 0.04 |
| Rectangle (type 1, small) | 0.8 |
| Rectangle (type 1, large) | 0.2 |
| Rectangle (type 2) | 0.5 |
| Ellipse | $1-\frac{\pi}{8}$ |
| Tube | 0 |
| Cube 3D | 0 |
| Sphere 3D | $1+\frac{\sqrt{8}}{3}\pi-\frac{5}{4}\pi$ |
| Tube 3D | 0 |

TABLE 1. Critical porosity value $\hat{\theta}$ of degeneration for geometries depicted in Figure 2 and 3.

tensor over the porosity is evaluated. In [18] the permeability depending on the saturation for fix porosity is computed for 2D rectangular cell geometries. In [52] the permeability is computed for some simple geometries, where the underlying cell problem is considered for several boundary conditions (periodic, uniform, confined). Numerical simulations and computations for the permeability in geometries with textile microstructures are considered in [24]. A numerical procedure for the evaluation of equivalent permeability for fractured vuggy porous media is investigated in [29]. The relationship of permeability and porosity in a 2D porous structure formed by regularly placed overlapping solid circles was numerically investigated in [38]. In [31] precipitation and dissolution in a three-dimensional pore throat with evolving aperture was simulated and for different dissolution scenarios permeability-porosity relations were numerically derived. Likewise [36] investigates the dependence of the Kozeny constant on porosity and the pore to throat size ratio for an periodic array of rectangular rods. This article concludes that such geometric information should be taken into account to enhance the applicability of the Kozeny-Carman equation. In these articles above the numerical computations are based on the Navier-Stokes equations at the pore scale. Contrarily, [54] used a volume averaging approach to compute the permeability in a 2D square setting. A homogenization method by asymptotic expansion, cf. Section 3.1, was applied in [13] to obtain the permeability for a periodic array of cylinders, were the cell problem was computed numerically by mixed finite elements. All the articles compared there numerical results with the Kozeny-Carman equation and concluded that the usability of this well-established relation depends strongly on the underlying geometry. In [55] permeability relations for numerous geometries composed of squares were computed by finite difference methods. Finally, numerical simulations on real data set have been considered, cf. e.g. [37].

Besides [13, 35], only qualitative evaluations of the permeability-porosity relation were given. In [13, 35] interpolation of the obtained data has been done to provide easy to use functional relations (polynomial of third or fourth order) for the permeability. We contribute exactly to this point and provide quantitative porosity-permeability relations of Kozeny-Carman or power law type based only on the various prescribed geometries, cf. Table 2–8. To this end, first the auxiliary cell problems and tensors of Section 3 are computed on representative elementary volumes.

The geometries depicted in Figure 2 and Figure 3 may serve as reasonable model systems for different soil structures. Quintard already states in [40] that two dimensional model systems fail particularly if unconsolidated anisotropic systems are considered. Consequently 3D model systems are discussed additionally. The circle, sphere, and ellipse for instance represent single grain or granular soils such as sandy soils or artificial model systems consisting of glass beads. In case that the sphere touches the boundary of the reference cell a primitive cubic packing is obtained. Rectangles on the other hand have widely been used to represent platy structures. In case that the rectangles touch the boundary of the elementary volume, a system of tubes is obtained. Likewise, cubes represents blocky soil, and cuboids represent prismatic soils respectively.

For the square/cube and circle/sphere the evolution is uniform in the direction of the axis and in radial direction, respectively. For the cross two different evolutions are taken into account. First a pure lengthening of the cross arms along their axes (type 1) and second an additional thickening of the cross arms while lengthening (type 2). Likewise, for rectangles of different, but constant height uniform evolution in width is considered (type 1). Moreover, rectangles of type 2 and the ellipse evolve uniformly in width and also in height. Finally, we consider tubes of varying thickness (which equates rectangles of constant width 1 with varying height).

In this research, we also calculate the permeability on a real data set obtained from the group of Stephan Peth, University of Kassel, Germany. It is a slice of a 3D microaggregate scan ($250 \times 250 \times 250$ pixels) which is further modified as depicted in Figure 4. A modification of a subset ($128 \times 128$ pixels) is made such that the pore space is connected to guarantee unique solvability of the cell problem (12). The porosity is $\theta \approx 58.9\%$.

As a discretization method for the underlying partial differential equations the local discontinuous Galerkin method is used on structured grids within the software M++ [57]. Discontinuous Galerkin methods generally use element-wise polynomial but globally discontinuous ansatz functions. The local discontinuous Galerkin method uses a mixed formulation where second (or higher) order equations are replaced with a system of first order equations by introducing auxiliary flux variables. For an analysis and detailed description of the used method for the Darcy equation we refer to [46, 47]. The Stokes equation is discretized as described in [16] and the Beavers–Joseph interface condition to couple free and Darcy flow is employed as in [45, 44].

The meshes for the 2D-geometries comprise $128 \times 128$ elements in two dimensions. Those in three dimensions comprise $16^3$ elements.

The data obtained is interpolated using a least square method. For given porosities $\theta_i$, $i = 1, \ldots, N$ and computed permeabilities $K_i$, $i = 1, \ldots, N$, we search for the parameter vector $\alpha^\star$ minimizing the sum of the least squares

$$\sum_{i=1}^{N} (f(\alpha, \theta_i) - K_i)^2$$

for one of the permeability functions $f = K_{KC1}, K_{KC2}, K_{KC3}, K_{VP}$, cf. (5)–(8), with different number $J = 1, 2, 3$ of parameters $\alpha_j \in \{\lambda, \beta, \eta\}$, $j = 1, \ldots, J$. For the isotropic geometries the permeabilities $K_i$ are given as the computed scalar-valued tensor. For the anisotropic geometries we chose $K_i$ as the eigenvalue that corresponds to the flow in the distinct direction in which no flow is possible at the critical porosity $\hat{\theta}$. For the tube in 3D we consider the eigenvalue corresponding to the flow alongside the tube (EV1) and additionally the eigenvalue corresponding to the flow orthogonal to the tube (EV2) because both tend to zero as $\theta$ tends to zero. The related minimization problem is solved in MATLAB2017a[1] by means of the routine **nlinfit**. The data points in our study were chosen with a minimum distance of 0.01 in the porosity $\theta$. For the 2D geometries, our data points are approximately equally distributed with the number of points $N$ depending on the critical porosity $\hat{\theta}$, ranging from $N = 15$ for the rectangle (type 1, small) to $N = 63$ for the tube. For

[1]©2017 The MathWorks, Inc. MATLAB and Simulink are registered trademarks of The MathWorks, Inc. See mathworks.com/trademarks for a list of additional trademarks. Other product or brand names may be trademarks or registered trademarks of their respective holders.

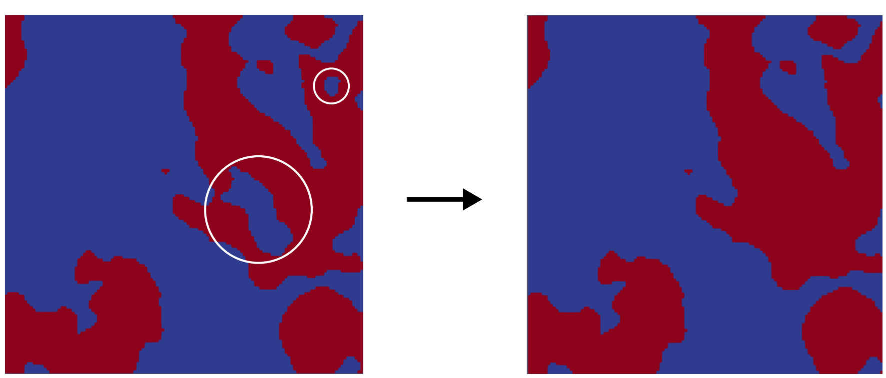

FIGURE 4. Modification of the geometry of a real porous medium from CT images; fluid in blue, solid in red. *Left*: original CT image, *Right*: modified geometry.

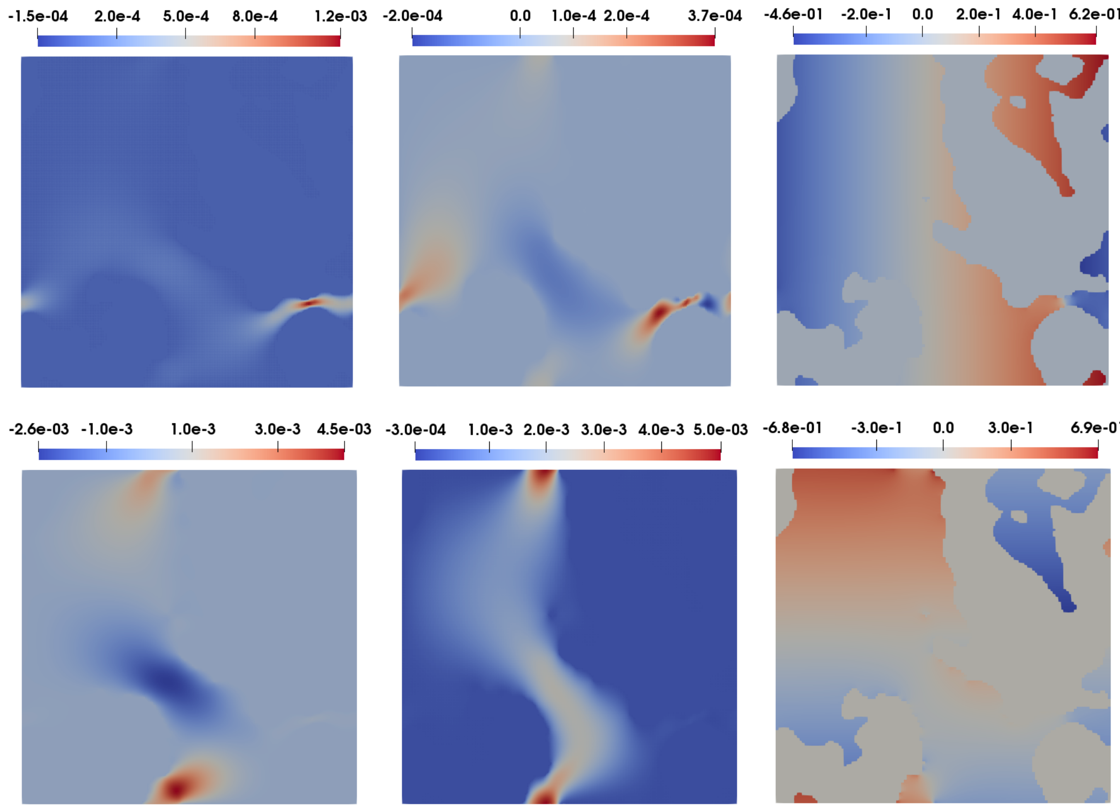


FIGURE 5. Cell problems' solutions on the real geometry depicted in Figure 4 with right hand side $e_1$ (*top*), and $e_2$ (*bottom*); $\omega_1$, $\omega_2$, $\pi$ from *left* to *right*.

the 3D geometries the data points are slightly weighted towards higher porosities. It should be noted, that we computed the data points for the 3D cube and tube with the obstacle placed in the corner of the cell instead of the center. This way we obtain an appropriate number of data points ranging from $N = 13$ for the cube to $N = 34$ for the sphere. In order to evaluate our fitting, we define the relative error as follows

$$e_{rel} = \frac{\sqrt{\sum_{i=1}^{N} \left(f(\alpha^*, \theta_i) - K_i\right)^2}}{\sqrt{\sum_{i=1}^{N} K_i^2}} .$$

## 5. EVALUATION

In this section, we evaluate the outcome of our numerical simulations. We first visualize the cell problems' solutions for a real geometry as depicted in Figure 4 and state the corresponding permeability tensor. Thereafter, we calculate porosity-permeability relations for various isotropic and anisotropic geometries as depicted in Figure 2 and 3. We compare our results with the well established Kozeny-Carman and Verma-Pruess relations, cf. Section 2, and provide quantitative functional relations of type (5)–(8) for the various geometries. Furthermore, we investigate the influence of a microporous solid matrix onto the permeability, which illustrates that even the full geometrical information generally does not suffices to determine the permeability.

5.1. **Simulation on real geometry.** The solutions of the Stokes cell problems (12) on the modified real geometry as depicted in Figure 4 are visualized in Figure 5. Integrating the flux solution, we obtain the permeability tensor

$$\mathbb{K} = 10^{-3} \begin{pmatrix} 0.02189 & 0.005866 \\ 0.005873 & 0.398 \end{pmatrix}$$

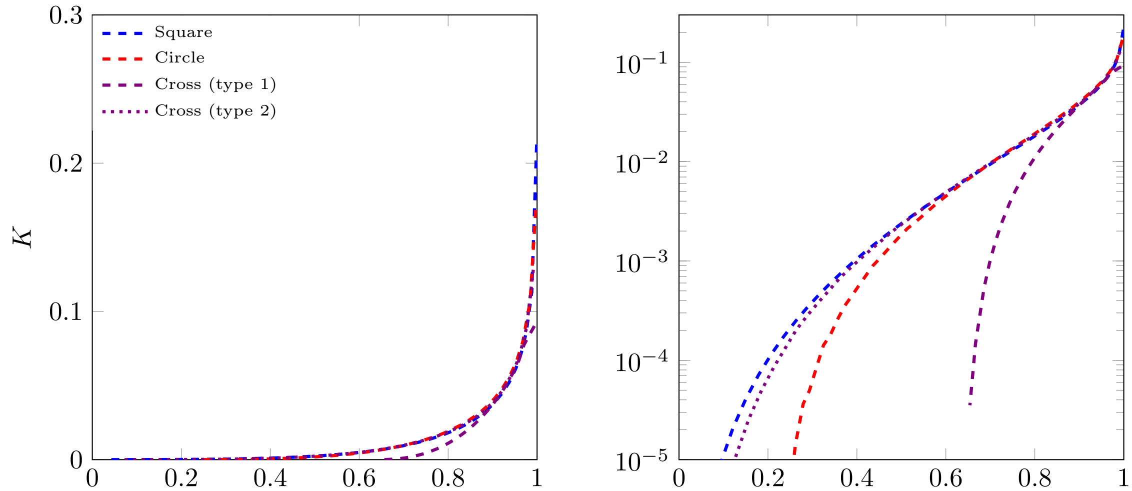


FIGURE 6. Scalar representative $K$ over porosity for isotropic geometries in 2D: square, circle, cross (type 1 and 2); *Left:* linear scale, *Right:* semi-logarithmic scale

with eigenvalues $\lambda_1 = 0.398 \cdot 10^{-3}$, $\lambda_2 = 0.0218 \cdot 10^{-3}$. The real geometry has a porosity of $\theta \approx 58.9\%$. For comparable porosity of $\theta \approx 58.5\%$, we obtain the permeability $K = 0.00442$ for a cross (type 2), which overestimates the calculated real geometry's permeability. On the other hand, the permeability $K = 0.0000353$, which we obtain for the cross (type 1) for a porosity of $\theta \approx 65.4\%$ underestimates the real geometry.

5.2. **Porosity-permeability relations.** In this section, we evaluate the permeability in terms of porosity for the representative geometries illustrated in Figure 2 and 3. Contrary to experimental capabilities, we thereby consider the whole range of porosities $0 < \theta < 1$, cf. discussion in Section 2. In Figure 6 the porosity-permeability relation is depicted for the chosen representative isotropic geometries, in Figure 7 for the chosen anisotropic geometries, and in Figure 8 for the chosen three dimensional geometries (anisotropic in case of the tube), respectively. We emphasize that depending on the chosen (anisotropic) geometry significantly different values are obtained for the effective permeability even assuming the same porosity values. In this sense it is evident that the underlying geometrical shape and structure plays an essential role for the porosity-permeability relation.

It is evident from Figure 6 and 7 that the permeability degenerates for values $\hat{\theta} > 0$ for some geometries and is not always singular in $\theta = 1$, but has finite value instead. This is because some geometries such as the square or circle shrink to a single point in the limit $\theta \to 1$ and thus yield a singularity. Contrarily, the tube, rectangle (type 1), and cross (type 1) have more complex geometrical 1D-limits for $\theta \to 1$ such as line segments or crosses with thickness 0. These limits are still obstacles and thus impede the fluid flow. As we will see below, for these geometries the exponental power 2 in the denominator in (1) exactly balances with the order of $\theta$-dependence of the specific surface $\sigma$, cf. (16a). In contrast, the three dimensional tube also shrinks to a line segment for $\theta \to 1$ which, however, does not affect the flow significantly, cf. Figure 8. Further note that the rectangle (type 1) with constant height $a$ coincides with the square for $\theta = 1 - a^2$, i.e. $\theta = 0.96$ for the rectangle (type 1, small) with $a = 0.2$ and $\theta = 0.36$ for the rectangle (type 1, large) with $a = 0.8$ in Figure 7. For these values the eigenvalues corresponding to the flow in vertical and horizontal direction, respectively, are equal and for $\theta < 1 - a^2$, i.e. if the rectangle width becomes larger than its height $a$, the eigenvalues change their ratio.

5.2.1. *Kozeny-Carman relation.* We now evaluate the Kozeny-Carman type equations (5)–(7) with different number of free parameters, cf. Section 2.

For the Kozeny-Carman equation (5) with **one free parameter** $\lambda$, Table 2 shows the least square fitting results for the geometries depicted in Figure 2 and 3 and evaluated in Figure 6 and 7. Moreover, the relative errors as introduced in Section 4 are calculated. The fitted values of $\lambda$ strongly vary for the different geometries ranging from $2.04 \cdot 10^{-7}$ to $3.4 \cdot 10^{-3}$. We emphasize that we have a bad approximation quality for all geometries as is evident from the calculated relative errors ranging from 44.8% to 89.1%, cf.

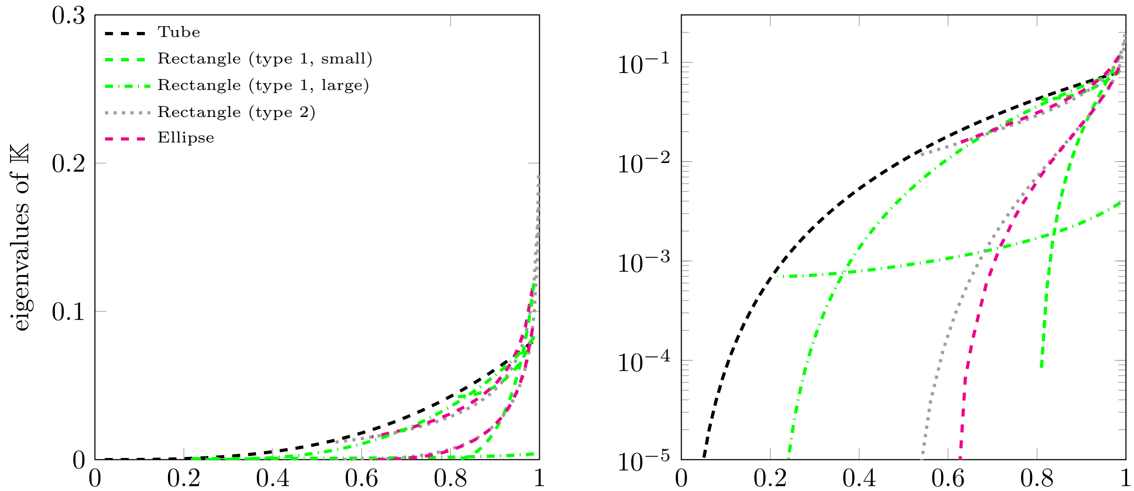


FIGURE 7. Eigenvalues of $\mathbb{K}$ over porosity for anisotropic geometries 2D: tube, rectangle (type 1, small and large), rectangle (type 2), ellipse; *Left:* linear scale, *Right:* semi-logarithmic scale

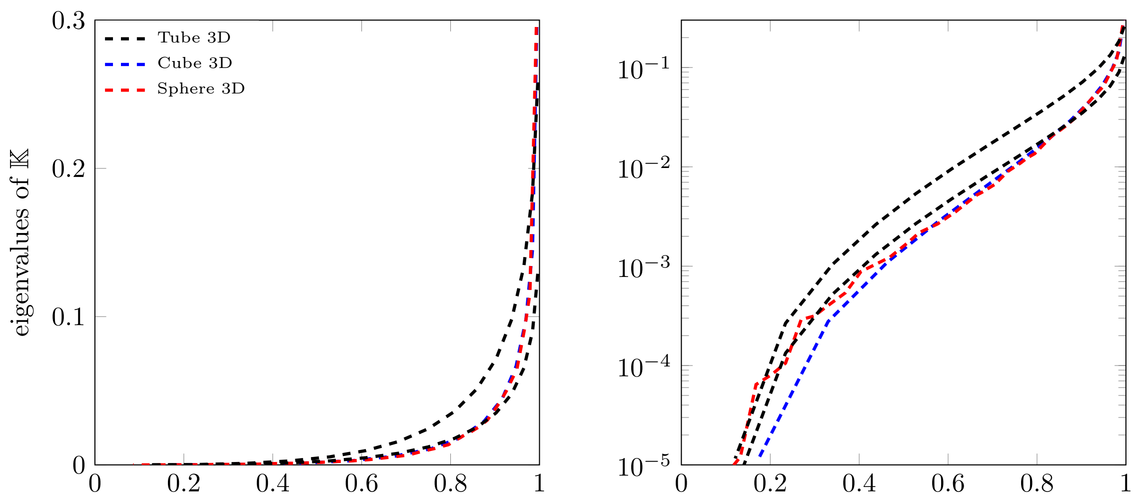


FIGURE 8. Eigenvalues of $\mathbb{K}$ over porosity for geometries in 3D: tube, cube and sphere; *Left:* linear scale, *Right:* semi-logarithmic scale

Table 2 and the illustration in Figure 9 (left). We conclude that this is due to the intrinsic dependence of the parameter $\lambda$ on the porosity $\theta$, cf. factor $\frac{c_0}{\sigma^2}$ in (1). However, for the one parameter model (5) the exponent of the denominator is fixed at value 2, which is not reasonable for most geometric shapes, see (16) below.

We next consider the Kozeny-Carman equation (6) with **two free parameters** $\lambda$ and $\beta$. In Figure 9 (right), we illustrate the approximation quality of the least square fits as given in Table 3. Although these fits show a much better approximation quality than the one parameter model (5), cf. Table 2 and Figure 9 (left), the largest relative error is still $e_{rel} = 8.76\%$ for the square, cf. Table 3. We emphasize that, on the other hand, the least square fit for the tube only has a marginal relative error of $e_{rel} = 0.003\%$, cf. Table 3 and Figure 9 (right, black lines). This is to be expected since the Kozeny-Carman relation (1) was originally derived for a bundle of tubes.

The values of the parameter $\beta$ range from $-0.0194$ to $0.482$, i.e. they are significantly smaller than the value of 2 which was proposed by Carman (1). We even obtain a slightly negative value of $\beta$ for the cross (type 1). In fact this $K_{KC2}$-fit would lead to an unreasonable degeneration of the permeability in the limit $\theta \to 1$. Since this has only impact for very large porosities, $\beta = 0$ would be a reasonable choice.

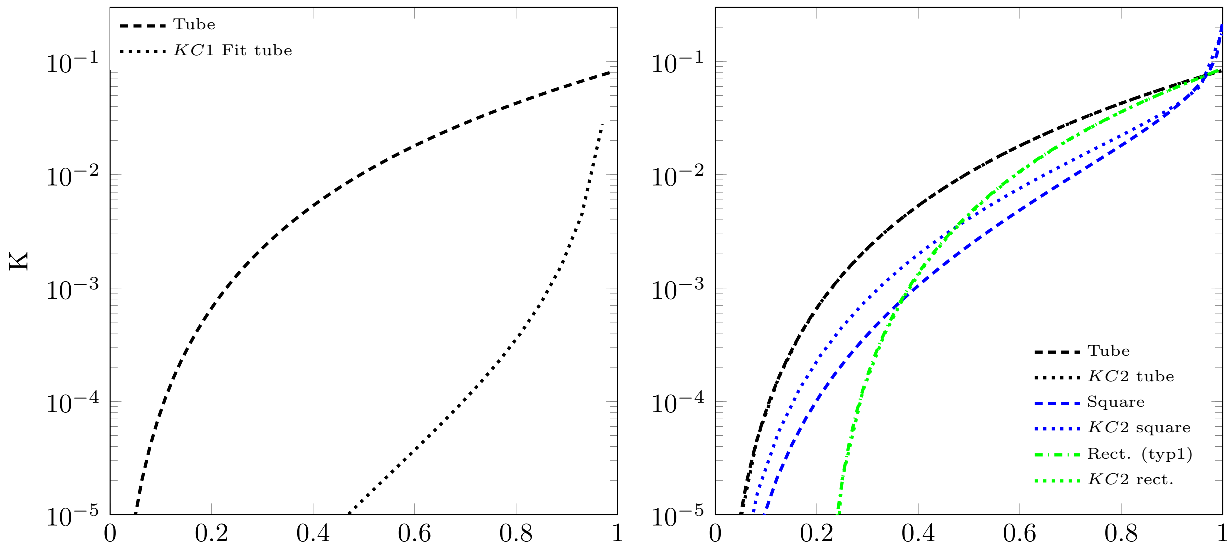


FIGURE 9. *Left:* least square fits of $K_{KC1}$ for tube, $\lambda = 0.0000275$ and $e_{rel} = 89.1\%$. *Right:* least square fits of $K_{KC2}$ for tube, square, and rectangle (type 1).

The obtained results are even more meaningful in the context of the Kozeny-Carman equation if it is taken into account that the prefactor $\frac{c_0}{\sigma^2}$ in (1) is in general not independent of the porosity $\theta$, cf. Section 2. We emphasize that the specific surface $\sigma$ indeed does depend on the porosity $\theta$ and consequently the exponential power of 2 in the denominator in (1) is reduced. More precisely, it holds with Kozeny constant $c_0 = \frac{1}{5}$

$$\begin{aligned}
\text{Square} : \sigma^2 &= \frac{16}{1-\theta} &\rightarrow \quad K &= \frac{1}{80}\frac{\theta^3}{1-\theta}\ , \\
\text{Circle} : \sigma^2 &= \frac{4\pi}{1-\theta} &\rightarrow \quad K &= \frac{1}{20\pi}\frac{(\theta-\hat{\theta})^3}{1-\theta}\ , \\
\text{Tube} : \sigma^2 &= \frac{4}{(1-\theta)^2} &\rightarrow \quad K &= \frac{1}{20}\theta^3
\end{aligned} \tag{16a}$$

| Geometry | $\lambda$ | $e_{rel}$ in % |
|---|---|---|
| Square | 0.000000204 | 69.4 |
| Circle | 0.00000365 | 72.8 |
| Cross (type 1) | 0.0000868 | 84.7 |
| Cross (type 2) | 0.0000121 | 72.0 |
| Rectangle (type 1, small) | 0.0034 | 64.9 |
| Rectangle (type 1, large) | 0.0000352 | 88.9 |
| Rectangle (type 2) | 0.00000598 | 73.3 |
| Ellipse | 0.000471 | 62.4 |
| Tube | 0.0000275 | 89.1 |
| Cube 3D | 0.00000139 | 46.7 |
| Sphere 3D | 0.00000154 | 44.8 |
| Tube 3D (EV1) | 0.00000417 | 68.5 |
| Tube 3D (EV2) | 0.00000208 | 67.8 |

TABLE 2. Least square fitted parameters and relative error for $K_{KC1}$.

| Geometry | $\beta$ | $\lambda$ | $e_{rel}$ in % |
|---|---|---|---|
| Square | 0.304 | 0.0266 | 8.76 |
| Circle | 0.301 | 0.0635 | 3.56 |
| Cross (type 1) | −0.0194 | 2.24 | 3.54 |
| Cross (type 2) | 0.380 | 0.0250 | 4.48 |
| Rectangle (type 1, small) | 0.0286 | 15.7 | 3.96 |
| Rectangle (type 1, large) | 0.0037 | 0.165 | 0.34 |
| Rectangle (type 2) | 0.313 | 0.201 | 4.34 |
| Ellipse | 0.298 | 0.476 | 1.88 |
| Tube | 0.0000218 | 0.0833 | 0.003 |
| Cube 3D | 0.459 | 0.0208 | 4.60 |
| Sphere 3D | 0.482 | 0.0201 | 4.71 |
| Tube 3D (EV1) | 0.300 | 0.0510 | 6.90 |
| Tube 3D (EV2) | 0.306 | 0.0245 | 6.22 |

TABLE 3. Least square fitted parameters and relative error for $K_{KC2}$.

and for the three dimensional geometries

$$\text{Cube 3D} : \sigma^2 = \frac{36}{(1-\theta)^{\frac{2}{3}}} \quad \to \quad K = \frac{1}{180}\frac{\theta^3}{(1-\theta)^{\frac{4}{3}}} \ ,$$

$$\text{Sphere 3D} : \sigma^2 \approx \frac{23.3867}{(1-\theta)^{\frac{2}{3}}} \quad \to \quad K \approx \frac{1}{116.9333}\frac{(\theta-\hat{\theta})^3}{(1-\theta)^{\frac{4}{3}}} \ ,$$

$$\text{Tube 3D} : \sigma^2 = \frac{16}{1-\theta} \quad \to \quad K = \frac{1}{80}\frac{\theta^3}{1-\theta} \ . \tag{16b}$$

We note that for the range $0.21 < \theta < 0.81$ the modified Kozeny-Carman relation (16b) for the three-dimensional tube lies in between the computed permeability curves for its eigenvalues EV1 (upper bound) and EV2 (lower bound) and is thus an adequate average approximation.

In case of the twodimensional tube, we conclude that $\beta = 0$ is the reasonable choice which perfectly fits our results, cf. Table 3. Moreover, the magnitude of the factor $\lambda = 0.0833$ fits quite well the proposed value $\frac{1}{20} = \frac{1}{4c_0} = 0.05$ with Kozeny constant $c_0 = \frac{1}{5}$ which was experimentally determined for diverse geometries. We conclude that the Kozeny-Carman relation (1) taking into account the specific surface (16a) accurately, perfectly approximates the geometry of tubes for which it was originally derived. The prefactor $c_0$ should further be related to tortuosity, cf. Section 2, which does not play a role for straight tubes and thus the permeability is underestimated (since $\lambda = 0.0833 > 0.05 = \frac{1}{4c_0}$), cf. Figure 10 (black lines). Finally, the analytically determined solution $K = \frac{1}{12}\theta^3$ for the Poiseuille flow in case of tubes, cf. [4] or Section 3.1, is perfectly reflected by the above computations, where $\beta \approx 0$ and $\lambda = 0.833 \approx \frac{1}{12}$.

Considering (16a), we rather expect $\beta \approx 1$, and $\lambda \approx \frac{1}{80} = 0.0125$ for the square and $\lambda \approx \frac{1}{20\pi} \approx 0.0159$ for the circle, respectively. In three dimensions (16b) suggests $\lambda \approx \frac{1}{80} \approx 0.0056$ and $\lambda \approx 0.0086$ with $\beta \approx \frac{4}{3}$ for the cube and the sphere, respectively. This yields a much better agreement compared to the approximations given for $\beta = 2$ (cf. Table 2 and 3).

We observe that the Kozeny-Carman equation often overestimates the permeability and note that the impact of tortuosity was completely neglected up to now. Therefore, in Figure 11 the numerically determined permeability and the Kozeny-Carman relation without and with the additional tortuosity factor $\frac{1}{\tau^2}$, cf. Section 2 are compared. We consider Archies law (2) with $n = 1$ leading to $\tau^2 = A\theta^{(1-m)}$ which has the most impact for the largest proposed parameters $A = 2$ and $m = 4$, see [17], i.e. $\tau^2 = 2\theta^{-3}$. It is evident from the Figures 11 and 12 that the permeabilities computed for the square and the circle belong to the area in between the Kozeny-Carman relation neglecting tortuosity and the relation with maximal tortuosity up to very large porosities, cf. gray areas in the Figures 11 and 12. This justifies a permeability-porosity relation by the Kozeny-Carman equation including the influence of tortuosity via Archies law (with an appropriate choice of parameters $A \leq 2$ and $m \leq 4$). Compared to the square, the mismatch of the Kozeny-Carman equation and the computed permeability is larger in case of a circle and increases for small porosities, cf. Figure 12. This is due to the fact that the circle has a positive critical porosity $\hat{\theta} = 1 - \frac{\pi}{4}$, cf. Table 1. Therefore, the

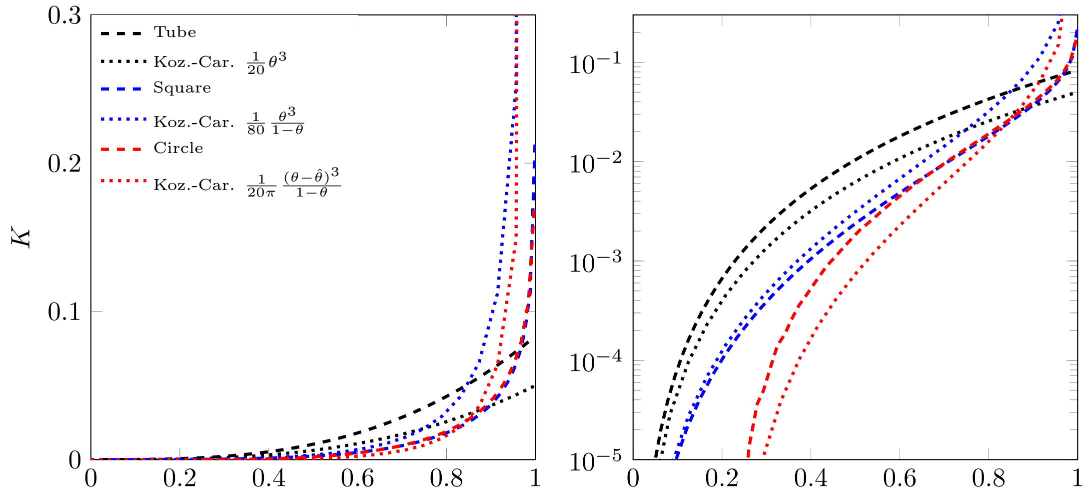


FIGURE 10. Scalar representative $K$ over porosity for tube, square, and circle compared with the corresponding Kozeny-Carman equation, cf. (16a); *Left:* linear scale, *Right:* semi-logarithmic scale

Kozeny-Carman relation taking this value into account (cf. Section 2) has better approximation quality than the original Kozeny-Carman equation (1), cf. Figure 12.

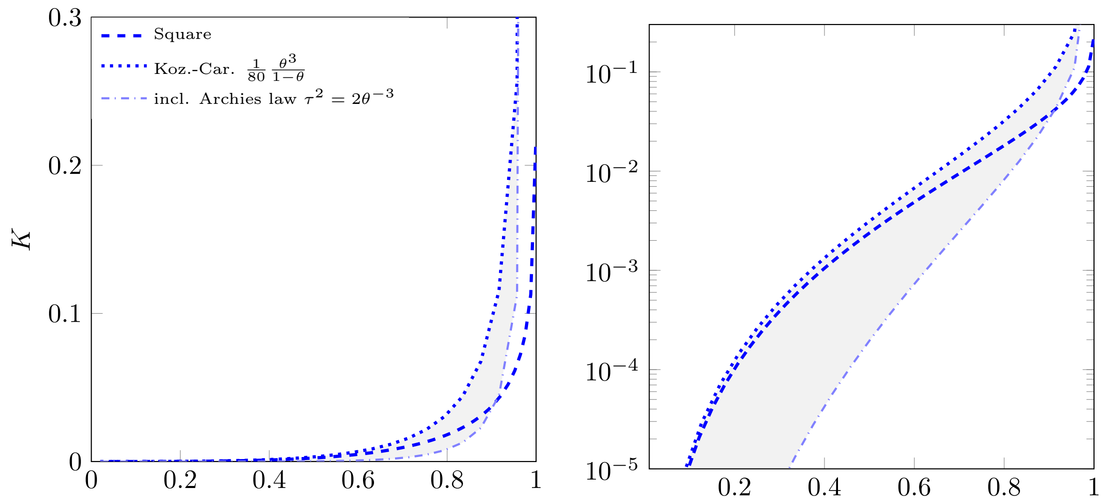


FIGURE 11. Scalar representative $K$ over porosity for the square compared with the corresponding Kozeny-Carman equation (16a); including Archies law (2); *Left:* linear scale, *Right:* semi-logarithmic scale

Finally, we consider the rectangle of type 1 with constant height $a$ or the cross of type 1 with constant cross arm thickness $a$. In both cases we obtain

$$\sigma^2 = 4\left(a + \frac{1-\theta}{a}\right)^2 \frac{1}{(1-\theta)^2} \quad \to \quad K = \frac{1}{20}\frac{a^2}{(a^2+1-\theta)^2}(\theta-\hat{\theta})^3 \tag{16c}$$

and conclude that in these situations the power law $\lambda(\theta-\hat{\theta})^3$ is reasonable since the singularity in $\theta = 1$ cancels out. Although the factor $\frac{1}{20}\frac{a^2}{(a^2+1-\theta)^2}$ still depends on the porosity, the influence of $\theta$ decreases for large $a$. Therefore, for both the cross (type 1) with $a = 1$ and the rectangles (type 1) particularly the large one with $a = 0.8$, the parameter $\beta$ is close to 0, i.e. $(1-\theta)^\beta \approx 1$, cf. Table 3. Consequently, for these

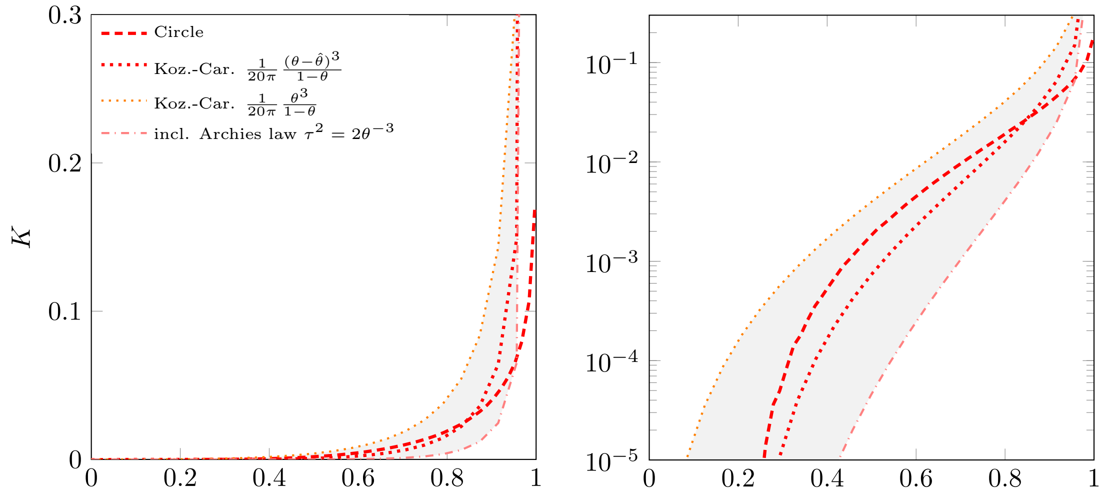


FIGURE 12. Scalar representative $K$ over porosity for the circle compared with the corresponding Kozeny-Carman equation (16a), with and without critical porosity $\hat{\theta}$ (cf. Table 1); including Archies law (2); *Left:* linear scale, *Right:* semi-logarithmic scale

| Geometry | $\beta$ | $\lambda$ | $e_{rel}$ in % |
|---|---|---|---|
| Square | 0.658 | 0.0124 | 0.70 |
| Circle | 0.267 | 0.0614 | 1.03 |
| Tube | 0.000161 | 0.0833 | 0.003 |
| Cube 3D | 0.987 | 0.00630 | 0.85 |
| Sphere 3D | 0.824 | 0.00850 | 2.90 |
| Tube 3D (EV1) | 0.704 | 0.0219 | 0.74 |

TABLE 4. Least square fitted parameters and relative error for $K_{KC2}$; restricted on the range $0 < \theta < 0.8$

specific geometries a power law $\lambda(\theta - \hat{\theta})^3$ is more suitable than the Kozeny-Carman equation. Because of this conclusion it makes sense to neglect the denominator and thus to use functional relations of power law type to fit the numerical results. This will be done in Section 5.2.2 below by investigating the Verma-Pruess equation $K_{VP}$.

If the range of porosity is restricted to $0 < \theta < 0.8$, the parameters $\beta$ and particularly $\lambda$ in the $K_{KC2}$-fit improve and better match with the values given in (16), cf. Table 4. We further note that the neglected range $0.8 < \theta \leq 1$, which contains the delicate point $\theta = 1$, is generally less important for applications. Finally, we consider the Kozeny-Carman equation $K_{KC3}$ with **three free parameters**. As expected, a comparison of Table 5 and Table 3 shows that the approximation quality increases with more fitting parameters. We estimate $\eta$ between 2.35 and 6.20 (see Table 5) for the least square fit. Regarding the tortuosity with respect to Archies law (2) the suggested exponent of 3 in the Kozeny-Carman relation may be enlarged. However, restricting the range of porosity to $0 < \theta < 0.8$ yields beside an improved agreement of the parameters $\beta, \lambda$ with (16) also exponents $\eta$, which are in a close range of the proposed value of 3, cf. Table 6. In particular, the averaged parameter $\bar{\eta} = 2.99$ of all considered geometries almost coincides with this value. The exponent of 3 consequently seems to be a good approximation for a wide range of geometries.

5.2.2. *Verma-Pruess relation.* We now investigate the Verma-Pruess relation (power law) $K_{VP}$. Table 7 shows the results of the least square fits for $K_{VP}$. Only for the cross (type 1), the rectangle (type 1), and the tube we obtain a good approximation quality with $e_{rel} \leq 4.34\%$, cf. Table 7. This result matches with the previous section, where precisely these geometries exhibits a parameter $\beta$ close to 0 justifying a power law approach. Especially for the tube the exponent $\eta$ is exactly equal to 3 verifying the results of Section

5.2.1, cf. Tables 3–5. Contrarily, the Verma-Pruess relation yields large relative errors ranging from 10.1% to 27.8% for all the other geometries. Therefore, it is not astonishing that the values for $\eta$ and $\lambda$ are ranging immensely up to 45.4 and 424.2, respectively, since the power law fits try with very high values of $\eta$ (ascent) and $\lambda$ (amount) to copy the singular behavior at $\theta = 1$, which is usually exhibited by the permeability tensor. Restricting the range of porosity to $0 < \theta < 0.8$ and thus disregarding a possible singularity at $\theta = 1$ decreases the fitted parameters $\eta \leq 5.05$, $\lambda \leq 0.925$ and the relative error $e_{rel} \leq 5.16\%$, cf. Table 8. Nevertheless, applying a power law the parameters also vary strong in the literature, cf. discussion in Section 2. Compared to these, the values of the exponent $\eta$ we obtained are still in a reasonable range.

5.3. **Comparison of the Stokes and the Stokes-Darcy regime.** As discussed above, there are diverse methods taking the dependence of the permeability on the underlying geometry into account. In the following we illustrate that even identical geometric settings may lead to different permeabilities. To this end, we study the impact of the porous matrix on the permeability. Also in such a situation the upscaling method enables us to calculate the permeability tensor $\tilde{\mathbb{K}}$, cf Section 3.2. Up to now, the porous matrix was considered to be inert, i.e. did not contribute to the permeability (Stokes regime). Contrarily, we now additionally assign a microporosity to the porous matrix (Stokes-Darcy regime). In Figure 14, we compare the cell problems' solution for the Stokes regime (11) with those of the Stokes-Darcy regime (15), cf. Section 3 where a representative microporous matrix (quadratic inclusion) $Y_d = [\frac{1}{4}, \frac{3}{4}] \times [\frac{1}{4}, \frac{3}{4}]$ is considered. Here, different values of permeability ranging from $\tilde{K} = 10^{-1}$ to $\tilde{K} = 10^{-7}$ are considered in the Darcy region. Grids of fineness $2^{-6}$ are used for the discretization as described in Section 4.

| Geometry | $\eta$ | $\beta$ | $\lambda$ | $e_{rel}$ in % |
|---|---|---|---|---|
| Square | 5.12 | 0.252 | 0.0375 | 3.06 |
| Circle | 3.53 | 0.276 | 0.0825 | 2.29 |
| Cross (type 1) | 2.69 | 0.0176 | 1.37 | 2.60 |
| Cross (type 2) | 4.08 | 0.318 | 0.0348 | 1.52 |
| Rectangle (type 1, small) | 2.35 | 0.162 | 3.02 | 0.26 |
| Rectangle (type 1, large) | 2.96 | 0.0090 | 0.160 | 0.14 |
| Rectangle (type 2) | 4.16 | 0.271 | 0.578 | 1.80 |
| Ellipse | 2.66 | 0.345 | 0.284 | 0.88 |
| Tube | 3.00 | −0.000263 | 0.0833 | 0.002 |
| Cube 3D | 6.20 | 0.405 | 0.0291 | 1.25 |
| Sphere 3D | 5.22 | 0.430 | 0.0299 | 1.32 |
| Tube 3D (EV1) | 5.28 | 0.226 | 0.0758 | 2.35 |
| Tube 3D (EV2) | 5.04 | 0.230 | 0.0350 | 2.11 |

TABLE 5. Least square fitted parameters and relative error for $K_{KC3}$.

| Geometry | $\eta$ | $\beta$ | $\lambda$ | $e_{rel}$ in % |
|---|---|---|---|---|
| Square | 3.28 | 0.533 | 0.0160 | 0.17 |
| Circle | 2.70 | 0.453 | 0.0390 | 0.26 |
| Cross (type 1) | 2.41 | 0.00720 | 0.909 | 0.04 |
| Cross (type 2) | 3.20 | 0.522 | 0.0195 | 0.19 |
| Rectangle (type 1, large) | 2.98 | 0.0035 | 0.1637 | 0.009 |
| Rectangle (type 2) | 2.99 | 0.530 | 0.110 | 0.008 |
| Ellipse | 2.50 | 0.345 | 0.220 | 0.73 |
| Tube | 3.00 | −0.0002 | 0.0834 | 0.001 |
| Cube 3D | 3.50 | 0.748 | 0.0101 | 0.13 |
| Sphere 3D | 2.59 | 1.01 | 0.00570 | 2.75 |
| Tube 3D (EV1) | 3.34 | 0.530 | 0.0306 | 0.07 |
| Tube 3D (EV2) | 3.35 | 0.520 | 0.0155 | 0.08 |

TABLE 6. Least square fitted parameters and relative error for $K_{KC3}$; restricted on the range $0 < \theta < 0.8$

| Geometry | $\eta$ | $\lambda$ | $e_{rel}$ in % |
|---|---|---|---|
| Square | 15.8 | 0.164 | 27.8 |
| Circle | 9.06 | 1.26 | 21.4 |
| Cross (type 1) | 2.79 | 1.64 | 2.77 |
| Cross (type 2) | 9.27 | 0.172 | 15.9 |
| Rectangle (type 1, small) | 3.00 | 17.4 | 4.34 |
| Rectangle (type 1, large) | 3.01 | 0.167 | 0.47 |
| Rectangle (type 2) | 11.5 | 424.2 | 17.3 |
| Ellipse | 4.87 | 9.42 | 10.1 |
| Tube | 3.00 | 0.0833 | 0.002 |
| Cube 3D | 45.4 | 0.377 | 18.4 |
| Sphere 3D | 39.4 | 1.53 | 21.3 |
| Tube 3D (EV1) | 12.3 | 0.242 | 14.1 |
| Tube 3D (EV2) | 12.6 | 0.120 | 14.9 |

TABLE 7. Least square fitted parameters and relative error for $K_{VP}$.

| Geometry | $\eta$ | $\lambda$ | $e_{rel}$ in % |
|---|---|---|---|
| Square | 4.45 | 0.0473 | 2.64 |
| Circle | 3.40 | 0.114 | 2.29 |
| Cross (type 1) | 2.42 | 0.925 | 0.04 |
| Cross (type 2) | 4.20 | 0.0564 | 2.29 |
| Rectangle (type 1, large) | 2.99 | 0.165 | 0.02 |
| Rectangle (type 2) | 3.47 | 0.450 | 1.06 |
| Ellipse | 2.71 | 0.539 | 0.97 |
| Tube | 3.00 | 0.0833 | 0.002 |
| Cube 3D | 5.05 | 0.0445 | 2.34 |
| Sphere 3D | 4.84 | 0.0506 | 5.16 |
| Tube 3D (EV1) | 4.35 | 0.0845 | 2.04 |
| Tube 3D (EV2) | 4.34 | 0.0419 | 2.00 |

TABLE 8. Least square fitted parameters and relative error for $K_{VP}$; restricted on the range $0 < \theta < 0.8$

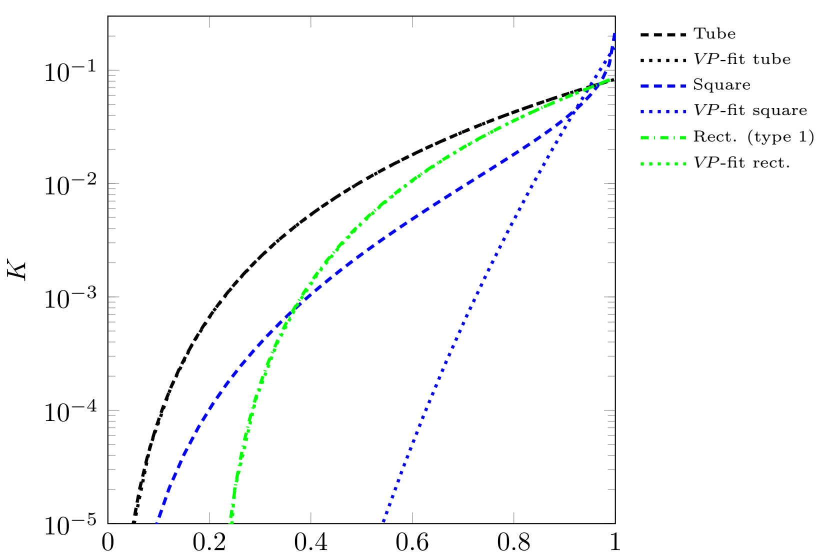


FIGURE 13. Least square fits of $K_{VP}$ for tube, square, and rectangle of type 1.

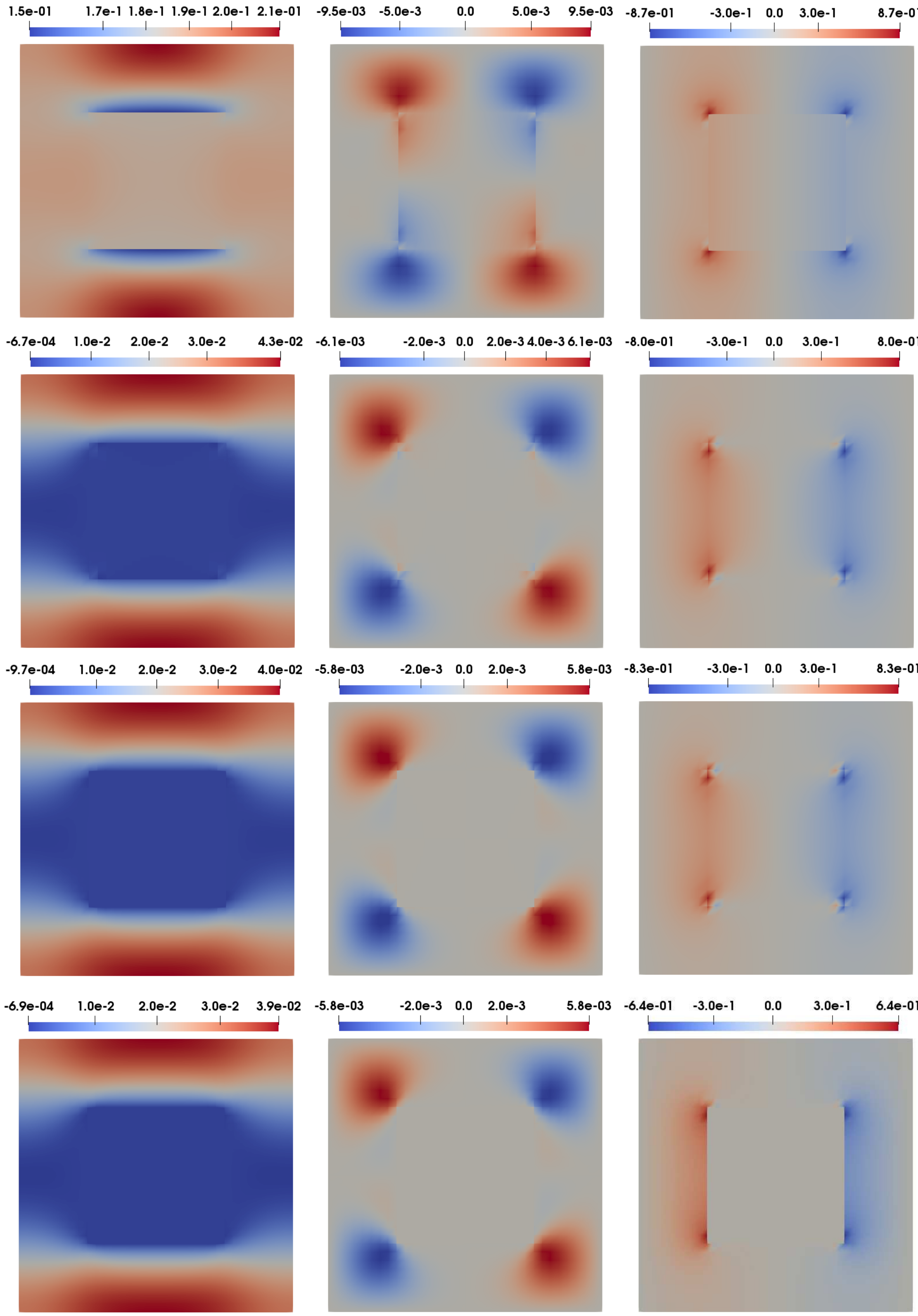


FIGURE 14. Cell problems' solutions $\omega_1$ (*left*), $\omega_2$ (*middle*) and $\pi$ (*right*) for Stokes-Darcy regime with right hand side $e_1$ and $\tilde{K} = 10^{-1}$ (*top*), $\tilde{K} = 10^{-4}$ (*2nd line*), $\tilde{K} = 10^{-7}$ (*3rd line*) and Stokes flow (*bottom*).

| $\tilde{K}$ | $10^{0}$ | $10^{-1}$ | $10^{-2}$ | $10^{-3}$ | $10^{-4}$ | $10^{-5}$ | $10^{-6}$ | $10^{-7}$ | $10^{-8}$ |
|---|---|---|---|---|---|---|---|---|---|
| $\bar{K}$ | 0.795 | 0.189 | 0.0436 | 0.0196 | 0.0149 | 0.0138 | 0.0135 | 0.0134 | 0.0134 |

Table 9. Permeability $\bar{K}$ of the Stokes-Darcy regime for different choices of $\tilde{K}$ in the porous matrix.

We compare the impact on the permeability values. For the Stokes regime, we calculate $K = 0.0131$ while Table 9 shows the different permeability $\bar{K}$ for the Stokes-Darcy regime ranging from 0.795 to 0.0134. It is evident that the impact of the Darcy regime is only negligible for small values of $\tilde{K}$ in the porous matrix.

## 6. Discussion

In this paper, standard results from upscaling theory were stated for a Stokes and Stokes-Darcy system. These results enable calculating the effective permeability tensor based on dynamically evolving representative elementary volumes. Fitting the data obtained, we provided quantitative relations between porosity and permeability of Kozeny-Carman and Verma-Pruess (power law) type. With our approach larger porosity ranges than accessible in experimental studies may be covered. Moreover, we were able to provide the full potentially anisotropic tensor (represented by its eigenvalues) instead of scalar representative which is only valid for isotropic situations. From our investigations, we conclude whether Kozeny-Carman type or power law type porosity-permeability relations are more reasonable for various prototypic representative elementary volumes. In doing so, we stress that the intrinsic dependence of the specific surface on the porosity can not be neglected in order to represent the strength of the singularity accurately. Restricting the range of porosity led to a decrease of the relative error of the fitted quantitative relations and moreover to a better agreement with the well-established parameters. Therefore, we expect that a sufficient restriction yields a very good match of these parameters. However, the goal of this article, beside others, was to provide quantitative relations depending only on the underlying geometry, which are valid in the whole (or slightly restricted) range of porosity. In this sense they generalize the well-established relations, which are commonly not applicable in the whole range.

Moreover, we demonstrated how our method may be applied to real geometries. Further research is needed to investigate porosity-permeability relations for larger three-dimensional samples. However, dynamic measurements are still challenging. A process driven understanding of the elementary volumes evolution is therefore essential to facilitate calculating the dynamic porosity-permeability relations.

Comprehensive flow and transport modeling also needs a parametrization of the effective diffusion tensor as proposed in [43]. Finally, further research including extension of homogenization results is needed to similarly approach the permeability in the unsaturated case.

## Acknowledgments

This research was kindly supported by the DFG RU 2179 “MAD Soil - Microaggregates: Formation and turnover of the structural building blocks of soils”. We acknowledge the group of Stephan Peth, University of Kassel, Germany, who provided the real 3D scan data.

## References

[1] Ahmadi, M.M., Mohammadi, S., Hayati, A.N.: Analytical derivation of tortuosity and permeability of monosized spheres: A volume averaging approach. Phys. Rev. E **83**, 8 (2011). DOI 10.1103/PhysRevE.83.026312
[2] Allaire, G.: Homogenization and two-scale convergence. SIAM J. Math. Anal. **23**(6), 1482–1518 (1992)
[3] Allaire, G., Brizzi, R., Dufrêche, J.F., Mikelić, A., Piatnitski, A.: Ion transport in porous media: Derivation of the macroscopic equations using upscaling and properties of the effective coefficients. Computational Geosciences **17**(3), 479–495 (2013). DOI 10.1007/s10596-013-9342-6
[4] Arbogast, T., Lehr, H.L.: Homogenization of a Darcy–Stokes system modeling vuggy porous media. Computational Geosciences **10**(3), 291–302 (2006). DOI 10.1007/s10596-006-9024-8
[5] Bear, J.: Dynamics of fluids in porous media. Dover Publications (1972)
[6] Beavers, G., Joseph, D.: Boundary conditions at a naturally permeable wall. J. Fluid Mech. **30**, 197–207 (1967)
[7] Bensoussan, A., Lions, J.L., Papanicolau, G.: Asymptotic analysis of periodic structures. North-Holland (1978)
[8] Berg, C.F.: Permeability description by characteristic length, tortuosity, constriction and porosity. Transport in Porous Media **103**(3), 381–400 (2014). DOI 10.1007/s11242-014-0307-6
[9] Bernabé, Y., Bruderer-Weng, C., Maineult, A.: Permeability fluctuations in heterogeneous networks with different dimensionality and topology. Journal of Geophysical Research: Solid Earth **108**(B7) (2003). DOI 10.1029/2002JB002326

[10] Carman, P.: Fluid flow through a granular bed. Trans. Inst. Chem. Eng. **15**, 150–167 (1937)
[11] Carman, P.: Permeability of saturated sands, soils and clays. Journal of Agricultural Science **29**, 263–273 (1939)
[12] Carrier, W.D.: Goodbye, Hazen; hello, Kozeny-Carman. Journal of Geotechnical and Geoenvironmental Engineering **129**(11), 1054–1056 (2003). DOI 10.1061/(ASCE)1090-0241(2003)129:11(1054)
[13] Chamsri, K., Bennethum, L.S.: Permeability of fluid flow through a periodic array of cylinders. Applied Mathematical Modelling **39**(1), 244 – 254 (2015). DOI 10.1016/j.apm.2014.05.024
[14] Chapuis, R.P.: Predicting the saturated hydraulic conductivity of soils: A review. Bulletin of Engineering Geology and the Environment **71**(3), 401–434 (2012). DOI 10.1007/s10064-012-0418-7
[15] Chapuis, R.P., Aubertin, M.: Predicting the coefficient of permeability of soils using the Kozeny-Carman equation. Can. Geotech. J. **40**(3), 616–628 (2003)
[16] Cockburn, B., Kanschat, G., Schötzau, D., Schwab, C.: Local discontinuous Galerkin methods for the Stokes system. SIAM Journal on Numerical Analysis **40**(1), 319–343 (2002). DOI 10.1137/S0036142900380121
[17] Costa, A.: Permeability-porosity relationship: A reexamination of the Kozeny-Carman equation based on a fractal pore-space geometry assumption. Geophysical Research Letters **33**(2), (L02,318) 1–5 (2006)
[18] Crolet, J.M.: Computational methods for flow and transport in porous media. Springer Netherlands (2000)
[19] Darcy, H.: Les fontaines publiques de la ville de Dijon. Exposition et application des principes à suivre et des formules à employer dans les questions de distribution d'eau: ouvrage terminé par un appendice relatif aux fournitures d'eau de plusieurs villes au filtrage des eaux et à la fabrication des tuyaux de fonte, de plomb, de tole et de bitume. Dalmont (1856)
[20] Duda, A., Koza, Z., Matyka, M.: Hydraulic tortuosity in arbitrary porous media flow. Phys. Rev. E **84**, 8 (2011). DOI 10.1103/PhysRevE.84.036319
[21] Dvorkin, J.: Kozeny-Carman equation revisited. Accessed: 15. Dec. 2016
[22] Galindo-Rosales, F.J., Campo-Deaño, L., Pinho, F.T., van Bokhorst, E., Hamersma, P.J., Oliveira, M.S.N., Alves, M.A.: Microfluidic systems for the analysis of viscoelastic fluid flow phenomena in porous media. Microfluidics and Nanofluidics **12**(1), 485–498 (2012). DOI 10.1007/s10404-011-0890-6
[23] Ghanbarian, B., Hunt, A.G., Ewing, R.P., Sahimi, M.: Tortuosity in porous media: A critical review. Soil Science Society of America Journal **77**, 1461–1477 (2013). DOI 10.2136/sssaj2012.0435
[24] Griebel, M., Klitz, M.: Homogenization and numerical simulation of flow in geometries with textile microstructures. Multiscale Model. Simul. **8**(4), 1439–1460 (2010). DOI 10.1137/09077059X
[25] Hallett, P., Karim, K., Bengough, A., Otten, W.: Biophysics of the vadose zone: From reality to model systems and back again. Vadose zone journal **12**(4), 17 (2013). DOI 10.2136/vzj2013.05.0090
[26] Hommel, J., Coltman, E., Class, H.: Porosity–permeability relations for evolving pore space: A review with a focus on (bio-)geochemically altered porous media. Transport in Porous Media **124**(2), 589–629 (2018). DOI 10.1007/s11242-018-1086-2
[27] Hornung, U.: Homogenization and Porous Media. Springer (1997)
[28] Huang, X., Yue, W., Liu, D., Yue, J., Li, J., Sun, D., Yang, M., Wang, Z.: Monitoring the intracellular calcium response to a dynamic hypertonic environment. Scientific reports **6**, 8 (2016). DOI 10.1038/srep23591
[29] Huang, Z., Yao, J., Wang, C.: Numerical calculation of equivalent permeability tensor for fractured vuggy porous media based on homogenization theory. Commun. Comput. Phys. **9**(1), 180–204 (2011)
[30] Kozeny, J.: Über kapillare Leitung des Wassers im Boden. Sitzungsber Akad. Wiss. Wien **136**(2a), 271–306 (2004)
[31] Li, X., Huang, H., Meakin, P.: A three-dimensional level set simulation of coupled reactive transport and precipitation/dissolution. International Journal of Heat and Mass Transfer **53**, 2908–2923 (2010). DOI 10.1016/j.ijheatmasstransfer.2010.01.044
[32] Menke, H., Bijeljic, B., Blunt, M.: Dynamic reservoir-condition microtomography of reactive transport in complex carbonates: Effect of initial pore structure and initial brine ph. Geochimica et Cosmochimica Acta **204**, 267 – 285 (2017). DOI 10.1016/j.gca.2017.01.053
[33] Nguetseng, G.: A general convergence result for a functional related to the theory of homogenization. SIAM Journal on Mathematical Analysis **20**(3), 608–623 (1989). DOI 10.1137/0520043
[34] Nimmo, J.: Porosity and pore size distribution. Encyclopedia of Soils in the Environment **3**, 295–303 (2004)
[35] van Noorden, T.: Crystal precipitation and dissolution in a porous medium: Effective equations and numerical experiments. Multiscale Model. Simul. **7**, 1220–1236 (2009)
[36] Ozgumus, T., Mobedi, M., Ozkol, U.: Determination of Kozeny constant based on porosity and pore to throat size ratio in porous medium with rectangular rods. Engineering Applications of Computational Fluid Mechanics **8**(2), 308–318 (2014). DOI 10.1080/19942060.2014.11015516
[37] Peszynska, M., Trykozko, A., Iltis, G., Schlueter, S., Wildenschild, D.: Biofilm growth in porous media: Experiments, computational modeling at the porescale, and upscaling. Advances in Water Resources **95**, 288 – 301 (2016). DOI https://doi.org/10.1016/j.advwatres.2015.07.008. Pore scale modeling and experiments
[38] Pinela, J., Kruz, S., Heitor Reis, A., Miguel, A., Aydin, M.: Permeability-porosity relationship assessment by 2d numerical simulations. Proceedings of the 16th international symposium on transport phenomena (2005)
[39] Pisani, L.: Simple expression for the tortuosity of porous media. Transport in Porous Media **88**(2), 193–203 (2011). DOI 10.1007/s11242-011-9734-9
[40] Quintard, M.: Diffusion in isotropic and anisotropic porous systems: Three-dimensional calculations. Transport in Porous Media **11**(2), 187–199 (1993). DOI 10.1007/BF01059634
[41] Randall, C.L., Kalinin, Y.V., Jamal, M., Manohar, T., Gracias, D.H.: Three-dimensional microwell arrays for cell culture. Lab on a Chip **11**(1), 127–131 (2011). DOI 10.1039/c0lc00368a
[42] Ray, N., van Noorden, T., Frank, F., Knabner, P.: Multiscale modeling of colloid and fluid dynamics in porous media including an evolving microstructure. Transp. Porous Media **95**(3), 669–696 (2012). DOI 10.1007/s11242-012-0068-z

[43] Ray, N., Rupp, A., Schulz, R., Knabner, P.: Old and new approaches predicting the diffusion in porous media. Transport in Porous Media **124**(3), 803–824 (2018). DOI 10.1007/s11242-018-1099-x
[44] Reuter, B., Rupp, A., Aizinger, V., Frank, F., Knabner, P.: Festung: A Matlab / GNU Octave toolbox for the discontinuous Galerkin method. Part IV: Generic problem framework and model-coupling interface (2018)
[45] Reuter, B., Rupp, A., Aizinger, V., Knabner, P.: Discontinuous Galerkin method for coupling hydrostatic free surface flows to saturated subsurface systems. Computers & Mathematics with Applications p. 19 (2019). DOI 10.1016/j.camwa.2018.12.020
[46] Rupp, A., Knabner, P.: Convergence order estimates of the local discontinuous Galerkin method for instationary Darcy flow. Numerical Methods for Partial Differential Equations **33**(4), 1374–1394 (2017). DOI 10.1002/num.22150
[47] Rupp, A., Knabner, P., Dawson, C.: A local discontinuous Galerkin scheme for Darcy flow with internal jumps. Computational Geosciences **22**(4), 1149–1159 (2018). DOI 10.1007/s10596-018-9743-7
[48] Shen, L., Chen, Z.: Critical review of the impact of tortuosity on diffusion. Chemical Engineering Science **62**(14), 3748–3755 (2004)
[49] Smith, M.M., Sholokhova, Y., Hao, Y., Carroll, S.A.: CO2-induced dissolution of low permeability carbonates. Part I: Characterization and experiments. Advances in Water Resources **62**, 370 – 387 (2013). DOI 10.1016/j.advwatres.2013.09.008
[50] Sobieski, W., Zhang, Q.: Sensitivity analysis of Kozeny-Carman and Ergun equations. Technical Sciences **17**(3), 235–248 (2014)
[51] Sullivan, R.R., Hertel, K.R.: The permeability methods for determining specific surface of fibers and powders. Advances in Colloid Science **1**, 37–80 (1942)
[52] Szymkiewicz, A.: Modelling water flow in unsaturated porous media: Accounting for nonlinear permeability and material heterogeneity. Springer (2012)
[53] Troeh, F.R., Jabro, J.D., Kirkham, D.: Gaseous diffusion equations for porous materials. Geoderma **27**(3), 239 – 253 (1982). DOI 10.1016/0016-7061(82)90033-7
[54] Valdes-Parada, F., Ochoa-Tapia, J., Alvarez-Ramirez, J.: Validity of the permeability Carman-Kozeny equation: A volume averaging approach. Francisco J. Valdes-Parada **388** (2009). DOI 10.1016/j.physa.2008.11.024
[55] Wang, Y., Sun, S.: Direct calculation of permeability by high-accurate finite difference and numerical integration methods. Communications in Computational Physics **20**(2), 405–440 (2016). DOI 10.4208/cicp.210815.240316a
[56] Whitaker, S.: The Method of Volume Averaging. Springer (1999)
[57] Wieners, C.: Distributed point objects. A new concept for parallel finite elements. In: T. Barth, M. Griebel, D. Keyes, R. Nieminen, D. Roose, T. Schlick, R. Kornhuber, R. Hoppe, J. Périaux, O. Pironneau, O. Widlund, J. Xu (eds.) Domain Decomposition Methods in Science and Engineering, *Lecture Notes in Computational Science and Engineering*, vol. 40, pp. 175–182. Springer Berlin Heidelberg (2005). DOI 10.1007/3540268251_14
[58] Yazdchi, K., Srivastava, S., Luding, S.: On the validity of the Carman-Kozeny equation in random fibrous media. In: E. Onate, D. Owen (eds.) PARTICLES 2011, pp. 1–10. ECCOMAS (2011)

# PREPRINTS

## DES INSTITUTS FÜR ANGEWANDTE MATHEMATIK (ISSN 1435-5833) BZW. (AB NR. 355) DES DEPARTMENTS MATHEMATIK (ISSN 2194-5127) DER UNIVERSITÄT ERLANGEN-NÜRNBERG

ZULETZT ERSCHIENENE BEITRÄGE:

384 M. Gahn, P. Knabner, M. Neuss-Radu: *Homogenization of reaction-diffusion processes in a two-component porous medium with a nonlinear flux condition at the interface, and application to metabolic processes in cells* (09.07.2014)

385 J. Jahn: *Directional derivatives in set optimization with the set less order relation* (08.08.2014)

386 N. Ray, P. Knabner: *Upscaling flow and transport in an evolving porous medium with general interaction potentials* (06.10.2014)

387 J. Greifenstein, M. Stingl: *Simultaneous material and topology optimization* (21.10.2014)

388 R. Schulz, N. Ray, F. Frank, H. Mahato, P. Knabner: *Strong solvability up to clogging of an effective diffusion-precipitation model in an evolving porous medium* (06.02.2015)

389 E. Bänsch, A. Brenner: *A-posteriori estimates for the rotational pressure-correction projection method* (29.05.2015)

390 M. Bischoff, J. Jahn: *Economic objectives, uncertainties and decision making in the energy sector* (07.10.2015)

391 R. Schulz, P. Knabner: *Derivation and analysis of an effective model for biofilm growth in evolving porous media* (08.03.2016)

392 M. Gahn, M. Neuss-Radu: *A characterization of relatively compact sets in* $L^p(\Omega, B)$ (29.04.2016)

393 N. Ray, A. Rupp, A. Prechtel: *Discrete-continuum continuum multiscale model for transport, biofilm development and solid restructuring in porous media* (26.09.2016)

394 J. Hoffmann, S. Kräutle, P. Knabner: *Existence and uniqueness of a global solution for reactive transport with mineral precipitation-dissolution and aquatic reactions in porous media* (15.11.2016)

395 N. Ray, R. Schulz, A. Rupp, P. Knabner: *Past and present approaches to calculate hydrodynamic parameters in evolving porous media* (16.12.2016)

396 M. Gahn, M. Neuss-Radu, P. Knabner: *Derivation of effective transmission conditions for domains separated by a membrane for different scaling of membrane diffusivity* (22.03.2017)

397 M. Gahn, M. Neuss-Radu, P. Knabner: *Effective transmission conditions for processes through thin heterogeneous layers with nonlinear transmission at the bulk-layer interface* (24.03.2017)

398 N. Ray, R. Schulz: *Derivation of an effective dispersion model for electroosmotic flow involving free boundaries in a thin strip* (31.05.2017)

399 A. Rupp, K.U. Totsche, A. Prechtel, N. Ray: *Discrete-continuum multiphase model for structure formation in soils including electrostatic effects* (28.05.2018)

400 N. Ray, J. Oberlander, P. Frolkovič: *Numerical investigation of a fully coupled micro-macro model for mineral dissolution and precipitation* (18.12.2018)

401 F. Frank, A. Rupp, D. Kuzmin: *Bound-preserving flux limiting schemes for DG discretizations of conservation laws with applications to the Cahn–Hilliard equation* (18.02.2019)

402 S. Kräutle, J. Hodai, P. Knabner: *Robust simulation of mineral precipitation-dissolution problems with variable mineral surface area* (04.03.2019)

403 R. Schulz, N. Ray, S. Zech, A. Rupp, P. Knabner: *Beyond Kozeny-Carman: Predicting the permeability in porous media* (20.03.2019)